Computer Modeling of Single-layer Nanocluster Formation in a Thin SiO2 Layer Buried in Si by Ion Mixing and Thermal Phase Decomposition

Prüfer, T.; Möller, W.; Heinig, K.-H.; Wolf, D.; Engelmann, H.-J.; Xu, X.; von Borany, J.;

Computer Modeling of Single-layer Nanocluster Formation in a Thin SiO$_2$ Layer Buried in Si by Ion Mixing and Thermal Phase Decomposition

Thomas Prüfer[1,a)], Wolfhard Möller[1], Karl-Heinz Heinig[1], Daniel Wolf[1,2], Hans-Jürgen Engelmann[1], Xiaomo Xu[1], Johannes von Borany[1]

[1]Helmholtz-Zentrum Dresden-Rossendorf, Dresden, Saxony, 01328, Germany
[2]Leibniz Institute for Solid State and Materials Research, Dresden, Saxony, 01069, Germany
[a)]Author to whom correspondence should be addressed: t.pruefer@hzdr.de

Abstract

A single sheet of Si nanoclusters with an average diameter of about 2 nm has been formed in a 30 nm Si / 7 nm SiO$_2$ / Si layer stack by 50 and 60 keV Si$^+$ ion-beam mixing at room temperature and fluences between $8.5 \cdot 10^{15}$ and $2.6 \cdot 10^{16}$ ions/cm^2, and subsequent thermal annealing at a temperature above 1000°C. Computer modelling of the process is accomplished by TRIDYN dynamic ballistic simulation of ion mixing and subsequent lattice kinetic Monte Carlo simulation of the phase decomposition of sub-stoichiometric silicon oxide into Si nanoclusters in a SiO$_2$ matrix. The simulation algorithms are briefly described with special emphasis on the choice of governing parameters for the present system. In comparison to the experimental results it is concluded that the predicted ion mixing profiles overestimate the interface broadening. This discrepancy is attributed to the neglect of chemical driving forces in connection with thermal-spike induced diffusion, which tends to re-constitute the Si/SiO$_2$ interfaces. With a corresponding correction and a suitable number of Monte Carlo steps, the experimentally obtained areal densities and average diameters of the nanoclusters are successfully reproduced.

1. Introduction

During the past decades, ion beam processing has gained renewed attention as a powerful tool for the production and modification of nanostructures with a large variety of functional properties[1,2]. Of special interest is the possibility of top-down production of nanocluster (NC) arrangements. For the present system, Si NCs have been generated in a SiO$_2$ matrix by ion implantation and thermal annealing for photoluminescence[3,4] and electroluminescence[5] studies, and to elaborate a non-volatile memory concept[6-9]. Alternatively, excess Si in SiO$_2$ as the precursor for NC formation can be obtained by ion-induced mixing at a Si/SiO$_2$ interface, from which Si nanoclusters are formed by subsequent thermal phase decomposition of the supersaturated oxide layer. This process has been applied to memory devices as well[10-12]. It has also been proposed for a novel fabrication approach for single electron transistors (SETs) operating at room temperature[13]. For this purpose, a Si NC with a diameter of a few nm shall be positioned in an oxide interlayer of less than 10 nm thickness in a

stacked Si/SiO$_2$/Si nanopillar of less than 20 nm diameter. This delicate arrangement requires an utmost precise control of the process parameters for ion irradiation and thermal phase decomposition. In a previous paper[14], we described a model system with local ion beam mixing being accomplished in a planar layer stack by Ne nanobeam irradiation in a He-Ne ion microscope device. For a production process being compatible with present-day complementary metal-oxide-semiconductor (CMOS) technology, basically two routes are available. (i) Arrays of stacked Si/SiO$_2$/Si nanopillars are prefabricated by lithography and etching, and subsequently subjected to ion irradiation and thermal annealing. (ii) Inverting the process sequence of (i), ion irradiation and annealing are applied to a planar layer stack prior to cutting out the nanopillars. The latter represents the most simple system in terms of computer simulation of ion beam mixing and subsequent phase decomposition.

In this view, the present work shall contribute to a detailed physical understanding of the ion-induced mixing and the subsequent thermal phase separation by advanced computer modelling. To describe the formation of the Si NCs in a planar Si/SiO$_2$/Si stack, a combination of ballistic computer simulation of ion beam mixing[15-17] and subsequent kinetic Monte Carlo simulation[8,9,18] of the thermal phase decomposition is employed. The role and the choice of critical parameters of the simulations will be discussed in detail with respect to their reliability. In comparison to experimental findings, the results will demonstrate that the ballistic simulation overestimates the ion mixing efficiency, which is attributed to a chemical effect.

2. Experimental

Samples have been cut from Si/SiO$_2$/Si wafers produced within the IONS4SET project[13] by thermal oxidation of [100] Si and subsequent liquid-phase chemical vapor deposition of amorphous Si, resulting in a top a-Si thickness of around 25 nm and an oxide interlayer thickness between 7 nm and 15 nm. In order to generate a solid solution of Si in the oxide interlayer by ion beam mixing, the samples have been irradiated with Si$^+$ ions with a flux of ~ 7·10^{12} ions/(s·cm²) at room temperature, energies between 50 keV and 60 keV, an angle of incidence of 7° with respect to the surface normal, and fluences up to several 10^{16} ions/cm^2. Subsequently, they have been annealed for phase decomposition of SiO$_x$ into Si NCs in a SiO$_2$ matrix by Rapid Thermal Annealing (RTA) at a temperature of 1050 °C for durations between 30 s and 60 s in a N$_2$ atmosphere.

To the best knowledge of the authors, there is no reliable quantitative experimental information available in literature on ion mixing in the Si/SiO$_2$ system. Appropriate diagnostics of the resulting compositional profiles require both sufficient depth resolution and sufficient sensitivity for the detection of Si in SiO$_2$ and/or O in Si. These are easily provided by Secondary Ion Mass Spectrometry

(SIMS), which, however, suffers from ion-induced distortion of the profiles and matrix effects[19]. X-ray induced photoelectron spectroscopy (XPS) depth profiling can hardly detect a 3 nm a-Si interlayer embedded in SiO_2 at a depth of 50 nm[20]. Cross-sectional Scanning Transmission Electron Microscopy (X-STEM) line-scan analysis may appear more promising at a first glance. However, in addition to the small low-Z sensitivity at the required depth resolution of less than 1 nm, energy-dispersive X-ray (EDX) analysis is disturbed by sideways oxidation of the cross-sectional lamella. Fitting et al.[21] applied electron energy loss spectrometry (EELS) to a 30 nm SiO_2 layer on Si after ion beam mixing, without, however, providing any quantitative dependence of the composition on depth. Similarly, own attempts for the present system did not yield any satisfactory results.
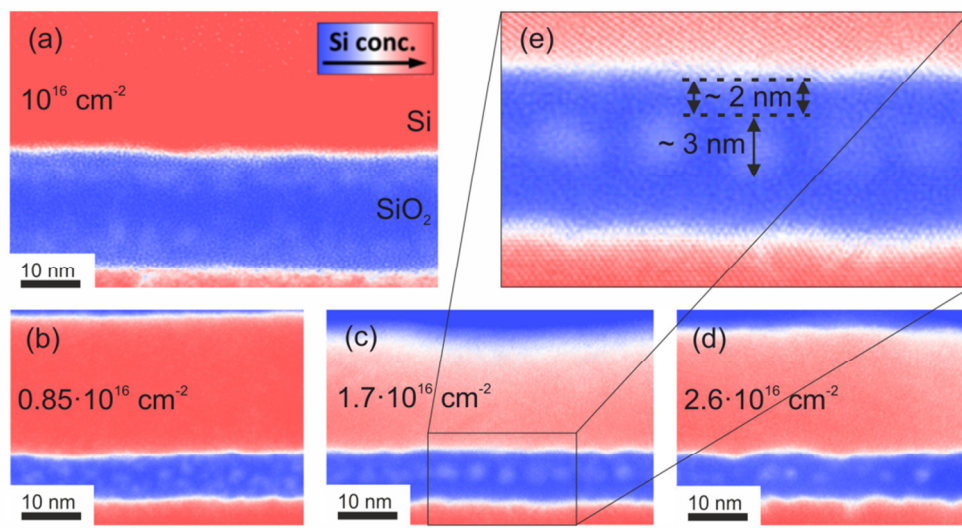

Figure 1: Si NC formation after Si^+ irradiation of a-Si / SiO_2 /c-Si layer stack at room temperature and the fluences indicated, and subsequent rapid thermal annealing at 1050 °C in a N_2 atmosphere. (a) top Si thickness 50 nm, oxide interlayer thickness 14 nm, ion energy 50 keV; (b-d) top Si thickness 30 nm, oxide interlayer thickness 7 nm, ion energy 60 keV; (e) zoom of (c). Annealing times were 30 s (a,c,d) or 60 s (b). The images show 2D projections of 3D structures in cross-sectional lamellas with an average thickness of 20…30

Thus, only the final morphology of precipitated Si obtained after ion beam mixing and thermal phase decomposition is accessible to reliable quantitative analysis. For this purpose, cross-sectional samples have been prepared by classical lamella preparation including sawing, grinding, polishing, dimpling, and final Ar^+ ion milling, or by Focused Ion Beam (FIB) milling in a Zeiss NVision 40 device. Energy-filtered transmission electron microscope (EFTEM) images have been recorded in a FEI Titan 80-300 microscope at an energy loss of 17 eV corresponding to the plasmon-loss peak of Si. Figure 1 shows selected examples. At a SiO_2 interlayer thickness of 14 nm (Figure 1(a)), two NC sheets form close to the interfaces, whereas a single sheet is formed in the center of the interlayer when shrinking its thickness to 7 nm (Figure 1(b-e)). Taking into account the local thickness of the cross-sectional lamella, which has been determined from transmission energy loss of 300 keV electrons in the TEM lamella[14], the areal density of NCs in the SiO_2 layer can be derived from the lateral

projections shown in Figure 1. In the following, we will concentrate on the system with an interlayer thickness of (7±0.5) nm. Table 1 reports the results obtained with different ion fluences. Only NCs with a minimum diameter of 1.5 nm have been taken into account.

Table 1: Experimentally observed areal densities and mean diameters of Si nanoclusters in an oxide interlayer with an initial thickness of 7 nm, after irradiation with 60 keV Si$^+$ ions at different fluences, and subsequent thermal annealing at 1050°C (see Figure 1).

Ion fluence (10^{16} cm^{-2})	0.85	1.7	2.6
Areal density (nm^{-2})	0.018	0.016	0.014
Mean diameter (nm)	1.96	2.23	2.23

3. Computer Simulation

3.1 Ballistic simulation of ion mixing

Compositional profiles after ion beam mixing have been obtained from TRIDYN dynamic ballistic computer simulations [15-17,22] based on the binary collision approximation (BCA). Briefly, the simulation traces the trajectories of incident ions and recoil atoms, which are generated in the associated collision cascades by binary atomic interactions in a screened Coulomb potential with the 'Kr-C' parametrization [23]. Energy transfer to the target electrons is modelled by an equipartition of local[24] and nonlocal[25] energy losses. For the dynamic alteration of the local composition, the target is initially split into thin depth intervals of thickness Δx_0 (for the present work, 500 intervals with $\Delta x_0 = 0.3$ nm thickness corresponding to a simulation depth of 150 nm). For each collision cascade initiated by a single incident ion, implanted ions are recorded as well as recoil atoms being sputtered from the surface or displaced in the bulk. Each 'pseudoatom' being involved in these processes alters the atomic areal density in the respective depth interval by a predefined amount ψ_0 (here, in the order of 10^{11} atoms/cm^2 per pseudoatom). Correspondingly, the thickness of each afflicted depth interval is relaxed after termination of the collision cascade, assuming fixed atomic volumes of the atomic constituents. At a resulting thickness $\Delta x < 0.5\,\Delta x_0$, the respective depth interval is combined with a neighboring one, at $\Delta x > 1.5\,\Delta x_0$ it is split into two depth intervals. Decreasing ψ_0 enhances the statistical quality of the simulation. For a predefined total ion fluence Φ_0, a total number $N_p = \Phi_0/\psi_0$ of pseudoprojectiles is run.

The probability of surface sputtering[26] depends critically on the choice of the surface binding energy (SBE). For elemental targets, the enthalpy of sublimation is generally accepted as a reasonable choice

of the SBE. For compounds, however, the definition is less straightforward. In TRIDYN, the actual SBE of a component i varies with the composition of the surface depth interval according to

$$U_s^{(i)} = \sum_{j=1}^{N_c} U_{ij} q_j \qquad i = 1, \ldots, N_c \tag{1}$$

where N_c denotes the number of atomic components, q_j the surface atomic fraction of component j ($\sum_j q_j = 1$), and U_{ij} are matrix elements describing binary interactions, which can be calculated from elemental enthalpies of sublimation, compound enthalpies of formation, and molecular binding energies in case of solid-gas compounds[17,27], resulting in $U_{SiSi} = 4.5$ eV, $U_{OO} = 0$, and $U_{SiO} = U_{OSi} = 12.8$ eV for the present system. This choice, however, underestimates experimental sputtering yields significantly[28]. In a detailed comparison of experimental sputtering yields[29,30] for Ar$^+$ irradiation of SiO$_2$ at keV energies with high-fluence TRIDYN results, we found reasonable agreement using $U_{SiO} = U_{OSi} = 2$ eV, which has also been employed in the present simulations.

Similarly, the efficiency of ion mixing depends on the threshold energy of atomic displacement in the bulk, U_d. Its definition is not straightforward. Tabulated data are available for crystalline materials at low damage levels[31-33]. However, most materials are highly damaged or even amorphized under ion irradiation at high fluences and sufficiently low temperatures, so that displacements may occur at lower energies due to trapping at preexisting defects. In their pioneering theoretical paper on ion mixing, Sigmund and Gras-Marti[34] propose a threshold energy of 7.8 eV for cascade mixing in Si. In consistence with this choice, a default setting of $U_d = 8$ eV has been successful in numerous ion mixing, preferential sputtering and thin film deposition studies using TRIDYN[27]. For SiO$_2$, element-specific values have recently been obtained from molecular dynamics (MD) computer simulation, with $U_d(Si) = 70.5$ eV and $U_d(O) = 28.9$ eV for quartz[35], and $U_d(Si) = 33.5$ eV and $U_d(O) = 16.3$ eV for amorphous SiO$_2$[36]. For crystalline Si, $U_d(Si) = 15$ eV[31]. In the present simulations, sub-stoichiometric SiO$_x$ (x<2) is treated as being composed from SiO$_2$ and additional Si. Correspondingly, employing the data pair for amorphous SiO$_2$, the displacement threshold energies are calculated in dependence on the local composition by linear interpolation, according to

$$U_d(Si) = 15\ eV + \frac{1}{2}\frac{q_O}{q_{Si}}(33.5\ eV - 15\ eV) \tag{2a}$$

with q_O and q_{Si} denoting the local oxygen and silicon atomic fractions, respectively, and

$$U_d(O) = 16.3\ eV \tag{2b}$$

3.2   Chemical effects on ion mixing

It is well established that ion mixing may be influenced by mechanisms other than purely ballistic relocation of atoms. The thermalization of the atomic motion in the collision cascade to mean energies in the eV and sub-eV regime results in local "thermal spikes"[37] by which thermal mobility can be transiently activated[38-42]. In chemically inert systems, ion mixing would thus be enhanced against the purely ballistic simulation. However, an additional influence may be exerted by chemical driving forces. For ion mixing in metallic bilayer systems, Johnson et al.[43-45] have developed a semi-empirical model of the influence of the cohesive energy and the mixing enthalpy. In endothermic systems with their tendency for phase separation, the mixing can even be reduced versus pure ballistic mixing. As it will be discussed to more detail in sect. 3.3, the solution of Si in SiO_2 is strongly endothermic. This may give rise to an effective uphill diffusion of Si and edge narrowing of the mixing profile. As already stated in sect. 2, any related information is not available in literature.

3.3   Kinetic Monte-Carlo simulation of thermal phase decomposition

For the simulation of the thermal phase decomposition with the ion mixing profiles from TRIDYN as input, a 3D lattice kinetic Monte Carlo simulation program has been employed[18], which has been adjusted and applied to different areas of ion surface interaction and surface physics[46-51]. Briefly, a homogeneous chemically inert matrix (here SiO_2) hosts atoms (here excess Si) either in the form of dissolved monomers or as precipitated clusters. The positions of the SiO_2 molecular species and the Si atoms are defined on a 3D lattice (an fcc lattice is used throughout this work with the lattice constant a_{fcc} adjusted to the Si density). Each lattice site hosts either a Si excess atom or half of a SiO_2 molecule, in order to approximately match the swelling factor 2.2 at the oxidation of silicon.

For the initial configuration, the respective 1D ion mixing profile obtained from TRIDYN, $q_{Si}(x)$, is converted into a Si excess profile according to

$$q_{Si}^{exc}(x) = \frac{n_{tot}(x)}{2n_{Si}^0}(3q_{Si}(x) - 1) \qquad (3)$$

with $q_{Si}(x)$ and $q_{Si}^{exc}(x)$ denoting the Si and Si excess atomic fractions, respectively, as function of the depth x, $n_{tot}(x)$ the total (Si+O) atomic density, and n_{Si}^0 the atomic density of crystalline Si. From this, in a preselected volume a random 3D distribution of excess Si atoms is created on the kMC lattice, which is consistent with the 1D depth distribution of eq. (3), and which contains sufficiently thick top and bottom layers where the kMC lattice is occupied with Si atoms only.

The kinetics is modelled as Kawasaki exchange processes between randomly selected nearest neighbor pair sites which are occupied by different species (Si or ½SiO_2) (see Figure 2). Using the

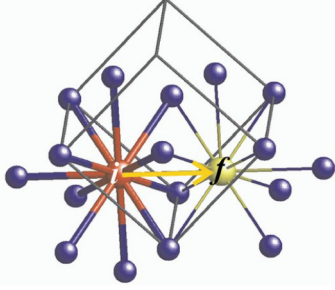Metropolis algorithm[52] in its simplest version, the probability of a successful Kawasaki exchange is given by

Figure 2: Nearest neighbor pair (NNP) *i-f* in a fcc lattice including its neighbor sites (blue). If *i* and *f* are occupied by different species (Si or ½SiO$_2$), then a Kawasaki exchange may occur with a certain probability in dependence on the resulting energy change of the NNP configuration which is given by the occupation of the blue surrounding atoms. In a first approximation, the energy of the NNP configuration can be assumed to be the sum of effective Si-Si bonds. However, to take into account the different solubilities of Si in SiO$_2$ and O in Si, the effective Si-Si bond energy depends on the fraction of each species in the NNP configuration.

$$W_{if} = \tau_0^{-1} \times \begin{cases} exp\{-\beta E_A\} & if \ n_f \geq n_i \\ exp\{-\beta[E_A + (n_i - n_f)E_b]\} & if \ n_f \leq n_i \end{cases} \tag{4}$$

with the exchange attempt frequency τ_0^{-1}, the activation energy of diffusion E_A, and $\beta = (k_B T)^{-1}$ with the Boltzmann constant k_B, the bond energy E_b and the temperature T. The nearest-neighbor (NN) site occupation numbers in the initial and final position of the jumping species is denoted by n_i and n_f, respectively. At constant E_A, it is convenient for simulation efficiency to normalize the exchange probability to the pure diffusion jump probability (upper case of eq. (4)) so that

$$W_{if}^* = \begin{cases} 1 & if \ n_f \geq n_i \\ exp\{-\beta[(n_i - n_f)E_b]\} & if \ n_f \leq n_i \end{cases} \tag{5}$$

with $\tau = \tau_0 exp\{\beta E_A\}$ representing the time scale of one MC step. Each MC step incorporates a sequence of N exchange attempts of statistically independently chosen atoms out of the full set of N atoms of the simulation cell. The number of exchange attempts corresponds to the number of atoms, so that on average each atom has the opportunity to perform one Kawasaki exchange per MC step. For a Si atom chosen, one of its surrounding NN sites is randomly selected for an attempt. If this site is not occupied by a ½SiO$_2$ species, another initial Si atom is randomly chosen in the simulation cell. An attempt is considered as successful if $r \leq W_{if}^*$ for a random number $r \in [0,1]$.

Equations (4) and (5) hold for binary systems with an essentially symmetric phase diagrams (i.e. the slope of the solidus is similar towards the two borders of the phase diagram), and with equal diffusivities of the minority phase of either species in the majority phase of the other species. In this case the kinetics can be described by one effective interatomic bond energy, e.g. $E_b = E_{Si-Si}$[53]. However, both the criteria of similar solidus slopes at the phase diagram borders and of similar

diffusivities of the minority phases are not fulfilled in the Si-SiO$_2$ system. Addressing diffusion first, E_A can be derived from the temperature dependence of experimentally determined diffusion coefficients $D = D_0 exp(-\beta E_A)$ with the pre-exponential factor D_0. The Monte Carlo step duration is then given by $\tau = (a^2/\xi)/D$ according to random walk theory, with a and ξ denoting the nearest neighbor distance and the coordination number in the fcc lattice, respectively. For Si in SiO$_2$ at 1000°C, most publications report rather low diffusion coefficients (smaller than 10^{-17} cm^{2}s^{-1} – see, e.g., refs. [54,55]), which may depend on the kind of SiO$_2$ (quartz, fused silica), and, e.g., on the location of the Si/SiO$_2$ interface. Even diffusion coefficients as small as 10^{-19} cm^{2}s^{-1} have been reported (see, e.g., ref. [56]). At the other boundary of the Si-SiO$_2$ phase diagram, the diffusivity of O (or ½SiO$_2$ species) in Si is orders of magnitude faster than the diffusion of Si in SiO$_2$, with a diffusion coefficient of about 10^{-11} cm^{2}s^{-1} at 1000°C[55,57].

In view of these widely different diffusivities, a special procedure has been adopted in the present simulations. The activation energy E_A and the temperature-dependent duration τ of the Monte-Carlo step are determined from the experimentally reported slow diffusivity of Si in SiO$_2$[57]. At the other border of the phase diagram the diffusion of O in Si is so fast that any rigorous definition of E_A and τ becomes meaningless. Instead, a kind of adiabatic approximation has been implemented: If there appears a lattice site occupied by a ½SiO$_2$ species with all nearest neighbor lattice sites occupied by Si, all the other kinetics is stopped, and a random walk of this particular species is performed until it attaches to a lattice site occupied by another ½SiO$_2$ species. This procedure approximates well the concentration-dependent diffusion in SiO$_x$ at the two borders of the phase diagram, so that it can be assumed to be valid for the entire composition range with $0 \leq x \leq 2$.

Going beyond the simple scheme of the Metropolis algorithm of eq. (4), specific bond energies may be sought for the pairwise Si-Si, Si-O and O-O interactions the SiO$_x$ system. In general, the values of the bond strengths E_{A-B} can be gauged by the solubilities of the respective atoms in the matrix[18]. Being determined at the two borders of the respective phase diagram, the bond strengths can then be interpolated over the entire composition range[50,53,58], provided that reliable data of the solubilities are available. Unfortunately, the phase diagram of SiO$_x$ is not well-known, especially not at the SiO$_2$ side. Therefore, in a simple approach, the three pair bond energies are assumed to be represented by one concentration-dependent Si-Si bond energy, $E_{Si-Si}(x)$ $(0 \leq x \leq 2)$. The effective bond energies $E_{Si-Si}(x = 0)$ and $E_{Si-Si}(x = 2)$ for the majority phases Si and SiO$_2$, respectively, can then be calculated from the corresponding solidus of the Si-SiO$_2$ phase diagram[18]. At the Si side, the solubility of O in Si at 1000°C amounts to several 10^{17} cm^{-3}, i.e. a few ppm[59-61]. Using the procedure described in ref.[18], we find a bond strength of $E_{Si-Si}(0) = 0.21\ eV$, or $\epsilon(0) = \frac{E_{Si-Si}(0)}{k_B T} = 1.95$ at 1050 °C. For the solubility of Si in SiO$_2$, there are much less reliable data. The only quantitative value

which we found in literature is based on a theoretical analysis by Sarikov[62], which, according to the author, is supported by a former theoretical study[63]. The reported solubility of Si in SiO_2 of $3...6 \cdot 10^{20}$ cm^{-3} at 1050°C, being in the 1% range, leads to $E_{Si-Si}(2) \approx 0.7\ eV$ or $\epsilon(2) > 6$. With this parameter being employed in phase separation simulations of an ion beam mixed Si/SiO_2 interfaces, SiO_2 NCs in the Si layer survive the thermal treatment longer than Si NCs in the SiO_2 layer. This is in contradiction to our former experimental studies[9,10] and the EFTEM images presented above, which demonstrate that the SiO_2 dissolve much faster so that only Si NCs survive. Thus, the solubility of O in Si is obviously higher than the solubility of Si in SiO_2. This is in contrast to the data given above, but in agreement with more recent – unfortunately only qualitative – statements that the solubility limit of Si in SiO_2 is "extremely low"[64,65]. In view of this absence of any reliable quantitative information, we have tested the results of the present kMC simulations against a reasonable variation of $E_{Si-Si}(2)$ with three values of 0.15, 0.21 and 0.27 eV, for which the solubilities of Si in SiO_2 are significantly higher than, equal to and significantly lower those of O in Si, respectively. With the border values $E_{Si-Si}(0)$ and $E_{Si-Si}(2)$ set in this way, the bond energies $E_{Si-Si}(x)$ for the entire composition range are calculated during the simulation by linear interpolation. The result is shown in Figure 3.
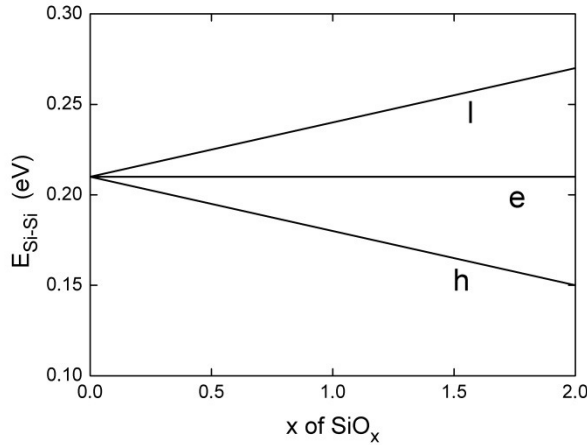

Figure 3: Concentration-dependent Si-Si bond strength used in the kMC simulations. The bond strengths in SiO_x are linearly interpolated between the limits Si and SiO_2. For these limits, the bond strengths are calculated from the solubility of O in Si and Si in SiO_2, respectively. As the solubility of Si in SiO_2 is not known, three values of $E_{Si-Si}(2)$ have been assumed, corresponding to widely different solubilities of Si in SiO_2, being lower than(l), equal to(e) and higher than(h) the solubility of O in Si.

3   Results and Discussion

Figure 4(a) shows the evolution of the compositional depth profile at increasing ion fluence for an initial oxide interlayer thickness of 7 nm, as obtained from TRIDYN ballistic computer simulation. As the collision cascades develop largely isotropic, forward and backward relocation of O at the lower and upper interfaces, respectively, are comparable, so that an almost symmetric broadening of the oxygen profile is observed. In addition, the profiles are shifted toward the surface mainly by surface sputtering of Si. A minor contribution results from Si being implanted behind the original oxide layer.

Figure 4(b) demonstrates a surprisingly small influence of the choice of the displacement threshold energies on the profile shape, although the composition-dependent energies according to eq. (2) are in average larger than the recommended general default value of 8 eV by a factor of about 2. Thus, the choice of the displacement threshold energy can be considered as uncritical in the present system.

The efficiency of ballistic ion mixing by the collision cascade versus depth x can be quantified by the mixing parameter[34]
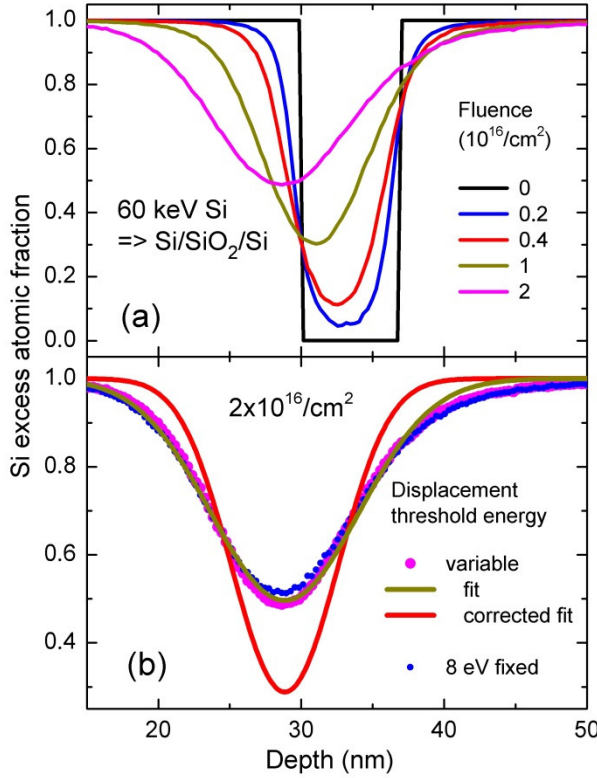

Figure 4: (a) Ion mixing profiles at increasing ion fluence of 60 keV Si[+] bombardment of a Si/SiO$_2$/Si layer stack with an initial oxide layer of 7 nm thickness centered at a depth of 33.5 nm (see Figure 1(c)). The displacement threshold energies have been chosen according to eq. (2). (b) Ion mixing profiles at a fluence of $2 \cdot 10^{16}$ cm^{-2} as in (a) (magenta dots), with a double error function fit according to eq. (9) (dark-yellow line), and the fit with corrected standard deviation (red line) (see Figure 8). In addition, the profile obtained with a fixed displacement threshold energy of 8 eV for both Si and O is shown (small blue dots).

$$M(x) = \int l^2 \frac{d\sigma(x,l)}{dl} dl \qquad (6)$$

where l denotes the component of the displacement vector along the depth of a recoil atom generated at x, and $d\sigma/dl$ the differential cross section for the generation of such a recoil. The mixing parameter can be obtained by recording the corresponding events during a static BCA computer simulation. For the experimental system of Figure 1(b-d), the result is shown in Figure 5. The mixing parameter $M(x)$ peaks at the position of the oxide interlayer due to the larger atomic density there; otherwise, it is fairly constant over the region of interest ($x \leq 60$ nm).

If the mixing results mainly from multiple displacement of recoil atoms in subsequently generated collision cascades, it can be described in analogy to diffusion in a solid[66]. For a bilayer system with a

sufficiently thick top layer of species A on a substrate B, with an interface originally positioned at depth x_0, the "diffusion" profile of A due to ion mixing is given by
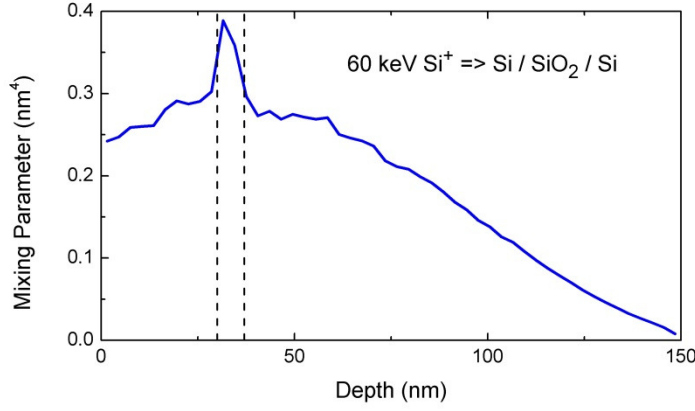

Figure 5: Mixing parameter for the initial layer stack as obtained from static TRIDYN simulation. The dashed lines indicate the position of the oxide interlayer.

$$q_A(x) = \frac{1}{2}\left(1 - erf\left(\frac{x - x_0}{\sigma_M}\right)\right) \tag{7}$$

where q_A is the atomic fraction of A, erf the error function, and σ_M the standard deviation. Compared to the conventional solution of the one-species diffusion equation, the standard deviation is enlarged by a factor of $\sqrt{2}$, as, during ion mixing, A is transported into B and vice versa. It is related to the mixing parameter and the ion fluence Φ by[34]

$$\sigma_M^2 = M \cdot \Phi \tag{8}$$

It should be noted that the diffusion approach neglects any shift[34] of the blurred interface, which is mainly caused by forward recoil implantation from the top layer. For the present Si/SiO₂/Si trilayer system, the mixing parameter is largely independent on depth as seen above. Further, the ballistic transport of Si into the oxide layer during irradiation is dominated by the large resources of the Si top and bottom layers, with only a minor contribution of additional Si already deposited in the interlayer. Therefore, the mixing profiles can be approximated by a superposition of two bilayer profiles according to eq. (7), resulting in

$$q_{Si}^{exc}(x, \Phi) = 1 + \frac{1}{2}\left(erf\left(\frac{x - x_2{}'(\Phi)}{\sigma_M(\Phi)}\right) - erf\left(\frac{x - x_1{}'(\Phi)}{\sigma_M(\Phi)}\right)\right) \tag{9}$$

where $x_1{}'$ and $x_2{}'$ denote the effective top and bottom interface depths, respectively, which deviate from the original depth due to surface sputtering, collision-induced shifts, and, to a minor extent, the implantation of incident Si ions as already stated above. Therefore, the mixing profiles as shown in Figure 4 have been fitted according to eq. (9) with the free parameters σ_M, $x_1{}'$ and $x_2{}'$. A typical

result is shown in Figure 4(b). The TRIDYN simulation data are well reproduced by the fit in particular with respect to the slopes of the blurred interfaces and the minimum Si atomic fraction. At the right shoulder, they lie somewhat below the symmetric fit curve. This can be attributed to forward recoil implantation of O from the oxide interlayer into the underlying Si bulk. At the selected fluence of $\Phi = 200$ nm^{-2}, the best fit value of the standard deviation, $\sigma_M = 6.76$ nm, is in reasonable agreement with eq. (8) with M being extracted from the initial distribution of the mixing parameter in the region of interest (see Figure 5). In addition, the fits for the different fluences reflect the dependence of eq. (8), $\sigma_M \sim \sqrt{\Phi}$, well (not shown). This confirms that the slopes of the simulated mixing profiles mainly result from multiple recoil displacement.
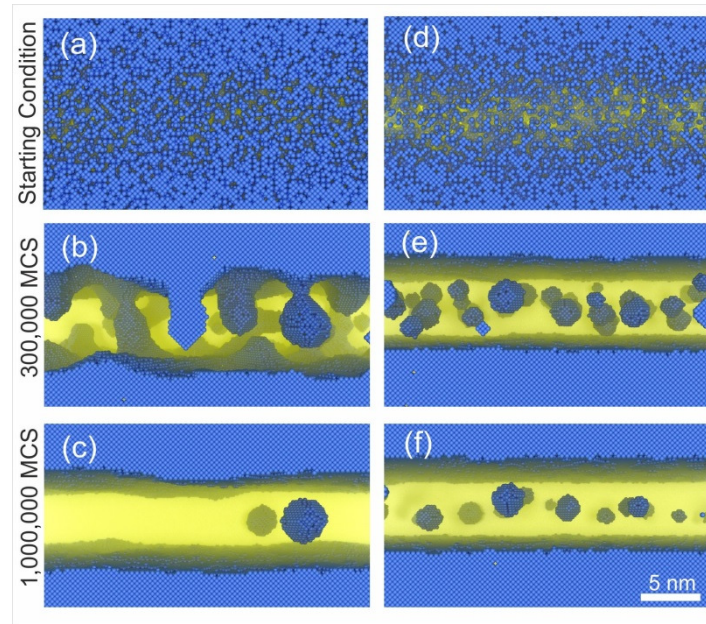

Figure 6: Si NC formation after ion mixing of a Si / SiO$_2$ / Si layer stack with top Si layer and oxide interlayer thicknesses of 30 nm and 7 nm, respectively, and subsequent thermal phase decomposition. The excess Si atoms and the SiO$_2$ species are colored in blue and yellow, respectively. (a),(d) SiO$_2$ layer blurring as predicted by TRIDYN simulations for 60 keV Si$^+$ irradiation at fluences of $1{,}7\cdot10^{16}$ cm^{-2} and $8.5\cdot10^{15}$ cm^{-2}, respectively, as converted into 3D distributions of excess Si atoms distributed over the kMC lattice (see text); (b),(c) and (e),(f) evolution of the initial distributions (a) and (b), respectively, as predicted by the kMC simulations after the indicated number of MC steps. The frames show 2D projections over a lateral thickness of 25 nm.

The ion mixing profiles generated by TRIDYN, represented by their fit functions according to eq. (9), are converted according to eq. (3) into a 1D distribution of excess Si atoms, from which a 3D distribution over the kMC lattice is randomly generated as the initial condition of the subsequent kMC simulation (see Figure 6(a) for an irradiation fluence of $1.7\cdot10^{16}$ cm^{-2}). The corresponding evolution of the system morphology during the kMC simulation, as obtained with $E_{Si-Si}(2) = 0.21\ eV$ (see sect. 3.2) is shown in Figure 6(b,c). (It should be noted that all excess Si, including Si NCs, in the oxide disappears at a sufficiently large number of MC steps due to re-integration at the

interfaces, which is not shown here. This is due to Oswald Ripening.). Apparently, the kMC simulation does not reproduce the morphology which has been observed experimentally after irradiation with the same fluence and subsequent thermal annealing (compare Figure 1(c) to Figures 6(b,c)). Whereas a single NC sheet with a rather regular lateral distribution of clusters is seen experimentally, the ion beam mixed SiO$_x$ layer evolves in the kMC simulation to a structure (see Figure 6(b)) which indicates a mechanism of spinodal phase decomposition[67] rather than of nucleation and growth[68,69], which would form isolated NCs in the matrix. At a later stage (see Figure 6(c)), a few large NCs separate from the previous spinodal-like structure.

For the kMC phase separation simulations, we note that at a given initial condition the development of the morphology depends in a unique way on the activation energy of Kawasaki exchanges and the bond strengths. For example, different jump activation energies result in a different time scaling of the simulation, but in essentially identical stages of the morphology evolution which just appear in different ranges of MC steps. We have confirmed this statement in numerous variations both of E_A and E_{Si-Si} [70] and, in the present simulations, for the variation of $E_{Si-Si}(2)$ as described in sect. 3.2. The morphology of Figure 6(b,c) is consistent with an excessive initial supersaturation of Si in the oxide layer resulting from the ion mixing simulation. Consequently, the nominal ion fluence of the latter has tentatively been reduced by a factor of 2, in order to artificially reduce the interface mixing (see Figure 6(d)). Indeed, Figure 6(e,f) demonstrates a good qualitative agreement with the morphologies found experimentally (Figure 1(c)). Here, phase separation proceeds via nucleation and growth rather than by spinodal decomposition, and the evolution of the excess Si distribution is governed by the slow Si diffusion through SiO$_2$, which leads to a Si NC layer embedded in SiO$_2$.

These findings suggest that the purely ballistic TRIDYN simulation of ion-induced mixing overestimates the interface broadening and thus produces an excessively large supersaturation of Si in the oxide interlayer. This is consistent with a reduction of the atomic mixing by thermal spike effects in endothermic systems, as described in sect. 2.2.

In order to formally adjust the TRIDYN results, we define for each irradiation fluence a correction factor $\alpha < 1$ to the standard deviation σ_M of the fit function $q_{Si}^{exc}(x)$ (see eq. (9)) for the respective mixing profile, by which the Si enrichment in the oxide layer is sufficiently reduced to yield an optimum agreement between the NC morphologies observed in the experiment and generated in the corresponding kMC simulation. As described in sect. 2, the experimentally observed NC morphology can be characterized quantitatively by (i) the mean diameter of the formed NCs and (ii) their areal density within the single NC sheet at a given irradiation fluence and annealing schedule. Both can be reproduced by a combination of the ballistic ion mixing simulation (with an appropriate correction factor α) and kMC phase separation simulation (with an appropriate choice of the number

of MC steps). This is demonstrated in Figure 7. With the TRIDYN result for $\Phi = 1.7 \cdot 10^{16}$ cm^{-2} as the origin, kMC simulations have been performed under variation of α. At increasing number of MC steps, NCs forms (after ~$0.5 \cdot 10^{16}$ MC steps) and their areal density (see Figure 7(a)) develops initially very quickly to a maximum. Subsequently, the small clusters merge by Ostwald ripening so that the areal density decreases. Then, around $8 \cdot 10^6$ MC steps in the present example, the desired NC sheet is formed, followed by a regime during which the NCs are gradually re-dissolved towards the final stable state with the Si/SiO$_2$/Si structure being re-established. During this course, the NC mean diameter (Figure 7(b)) first increases, and decreases then slowly prior to the formation of the NC sheet. There is a unique pair of the number of MC steps and the correction factor α which reproduces the experimental findings.
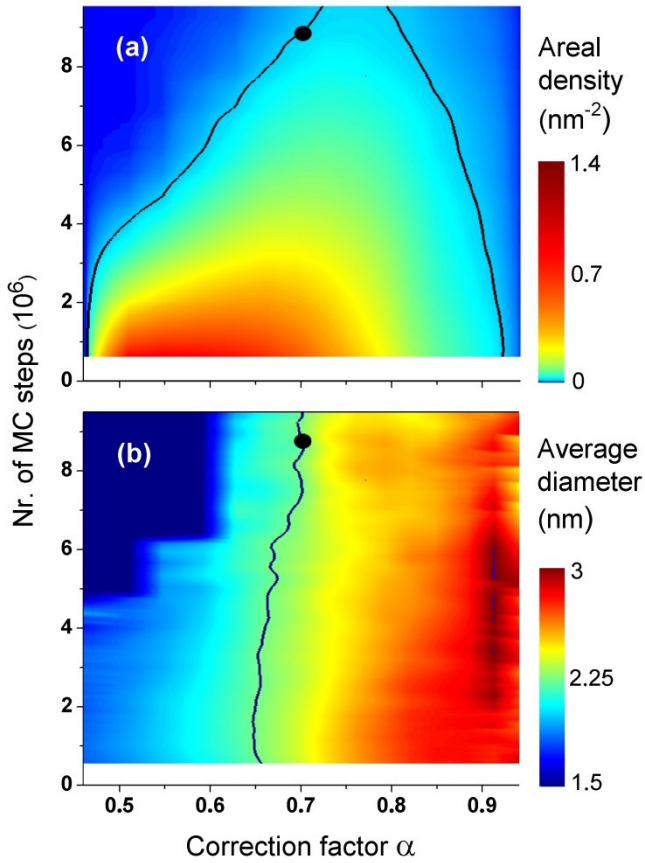

Figure 7: Si NC areal density (a) and average diameter (b) for the layer stack and the irradiation conditions of Figure 1(c) (60 keV, $1.7 \cdot 10^{16}$ /cm²). The color plots result from kMC simulation of phase decomposition based on the ballistic mixing profile obtained from TRIDYN, with different correction factors α to the standard deviation σ_M of the mixing profile (see eq. (9)) and increasing numbers of MC steps. The experimental areal density and average diameter of the nanoclusters (see Table 1) are marked in (a) and (b), respectively, as black isocontour lines. A unique combination of α and nr. of MC steps fits the experimental data as shown by the black dots.

The correction factors determined in this way are shown in Figure 8 for the different fluences of Figure 1(b-d). Figure 8 further demonstrates that the results – and thereby the results of the kMC simulations – depend only weakly on the choice of $E_{Si-Si}(2)$ (see sect. 2.3), although the corresponding solubilities of Si in SiO$_2$ are widely different. It appears that the TRIDYN simulations overestimate the widths of the falling and rising edges of the mixing profiles increasingly at increasing fluence. With the correction factor taken from Figure 8 for $E_{Si-Si}(2)$ = 0.21 eV and the

fluence of $2 \cdot 10^{16}$ cm^{-2}, Figure 4(b) shows the corrected fit profile, demonstrating a significant reduction of Si enrichment in the original oxide layer versus the purely ballistic TRIDYN simulation.

The dependence of the correction factor α on the irradiation fluence is less obvious. A potential qualitative explanation can be given in the following way: In the diffusion picture, the differential broadening of the ballistic mixing profile is given by[43]
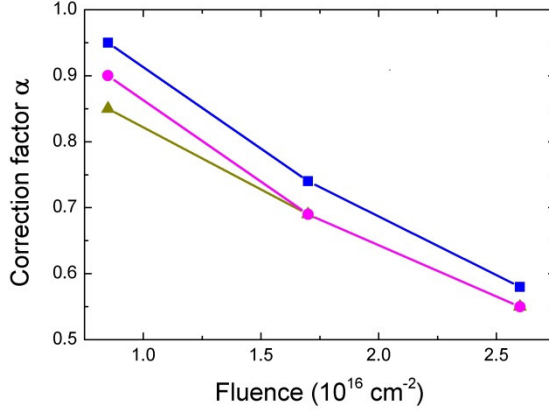

Figure 8: Correction factor α for different irradiation fluences (see Figure 1(b-d)), as obtained with three different bond strengths $E_{Si-Si}(2)$ of 0.15 eV (squares), 0.21 eV (circles) and 0.27 eV (triangles) in the kMC simulations (see Figure 3).

$$\frac{\partial \sigma_M^2}{\partial t} = 4D_M \tag{10}$$

with the irradiation time t and the diffusion coefficient D_M. Then according to eq. (8) and with j denoting the ion flux

$$D_M = \frac{M}{4}\frac{\partial \Phi}{\partial t} = \frac{M}{4}j \tag{11}$$

Thus, at constant j, the ballistic broadening depends only on the mixing parameter M of eq. (6). At increasing ion fluence, the zone of oxygen enrichment moves towards the surface due to sputtering, as seen in Figure 4, and thus into a regime of decreasing mixing parameter (see Figure 5), so that also D_M decreases. Both recoils of relatively high energy, which dominate the ballistic mixing, and collisional thermal spikes are basically generated by the deposition of the ion energy into atomic motion and thus follow a distribution similar to the one shown in Figure 5. However, the thermal spikes mainly occur in the final phase of the collision cascade, which is in average located at a larger depth than the depth of generation of recoils of higher energy. There, as indicated in Figure 5, the influence of any shift to the surface is smaller. Thus, the atomic mobility induced by thermal spikes will remain approximately stable, whereas the ballistic one is slightly reduced. Therefore, the relative influence of thermal spikes increases at increasing fluence, in qualitative agreement with the result of Figure 8. However, the phase separation, being a nonlinear process with respect to

supersaturation, may also influence the observed behavior. At increasing fluence, ion mixing results in an increasing supersaturation of Si in the oxide layer, so that the chemical driving forces may increasingly restore the interfaces in a nonlinear manner.

5.   Conclusions

A single Si nanocluster sheet has been formed in a SiO_2 layer of 7 nm thickness buried in Si using ion-beam induced atomic mixing at room temperature and subsequent thermal annealing at a temperature above 1000°C. The present work demonstrates that this process can be successfully modelled by dynamic ballistic computer simulation in the binary-collision approximation and subsequent kinetic lattice Monte Carlo simulation. However, the ballistic simulation overestimates the interface broadening by ion mixing. This is attributed to chemical driving forces in connection with thermal-spike induced mobility, which tends to re-constitute the Si/SiO_2 interfaces due to the strongly endothermic solubility of Si atoms in SiO_2. The influence of this mechanism increases at increasing ion fluence. Consequently, in comparison to the combined TRIDYN and kMC simulations, a larger ion mixing fluence is to be applied experimentally in order to obtain the predicted nanocluster morphology.

The results provide a semi-quantitative understanding of the process mechanisms and narrow down the parameter regimes of ion irradiation and thermal treatment. They are expected to be helpful for the modelling and understanding of single nanocluster formation in a $Si/SiO_2/Si$ stack in a nanopillar. Such work is in progress.

References

1   J. E. E. Baglin, Applied Surface Science **258,** 4103 (2012).
2   A. Johannes, H. Holland-Moritz, and C. Ronning, Semiconductor Science and Technology **30** (2015).
3   T. Shimizuiwayama, K. Fujita, S. Nakao, K. Saitoh, T. Fujita, and N. Itoh, Journal of Applied Physics **75,** 7779 (1994).
4   B. G. Fernandez, M. Lopez, C. Garcia, A. Perez-Rodriguez, J. R. Morante, C. Bonafos, M. Carrada, and A. Claverie, Journal of Applied Physics **91,** 798 (2002).
5   V. Beyer, B. Schmidt, K. H. Heinig, and K. H. Stegemann, Applied Physics Letters **95** (2009).
6   K. H. Heinig, T. Muller, B. Schmidt, M. Strobel, and W. Moller, Applied Physics a-Materials Science & Processing **77,** 17 (2003).
7   T. Muller, K. H. Heinig, and W. Moller, Materials Science and Engineering B-Solid State Materials for Advanced Technology **101,** 49 (2003).
8   T. Muller, K. H. Heinig, and W. Moller, Applied Physics Letters **81,** 3049 (2002).
9   T. Muller, K. H. Heinig, W. Moller, C. Bonafos, H. Coffin, N. Cherkashin, G. B. Assayag, S. Schamm, G. Zanchi, A. Claverie, M. Tence, and C. Colliex, Applied Physics Letters **85,** 2373 (2004).
10 L. Rontzsch, K. H. Heinig, and B. Schmidt, Materials Science in Semiconductor Processing **7,** 357 (2004).
11 L. Rontzsch, K. H. Heinig, B. Schmidt, A. Mucklich, W. Moller, A. Thomas, and T. Gemming, Physica Status Solidi a-Applications and Materials Science **202,** R170 (2005).
12 P. Dimitrakis, P. Normand, E. Vontitseva, K. H. Stegemann, K. H. Heinig, and B. Schmidt, in *Second Conference on Microelectronics, Microsystems and Nanotechnology*; *Vol. 10*, edited by A. G. Nassiopoulou, N. Papanikolaou, and C. Tsamis (2005), p. 7.
13 IONS4SET: Ion-irradiation-induced Si nanodot self-assembly for hybrid SET-CMOS technology, Project funded by the European Union, http://www.ions4set.eu/.
14 X. M. Xu, T. Prufer, D. Wolf, H. J. Engelmann, L. Bischoff, R. Hubner, K. H. Heinig, W. Moller, S. Facsko, J. von Borany, and G. Hlawacek, Beilstein Journal of Nanotechnology **9,** 2883 (2018).
15 W. Moller and W. Eckstein, Nuclear Instruments & Methods in Physics Research Section B-Beam Interactions with Materials and Atoms **7-8,** 645 (1985).
16 W. Moller, W. Eckstein, and J. P. Biersack, Computer Physics Communications **51,** 355 (1988).
17 W. Möller and M. Posselt, TRIDYN_FZR User Manual, Report FZR-317, Forschungszentrum Rossendorf (2001); https://www.hzdr.de/db/Cms?pOid=21578&pNid=0.
18 M. Strobel, K. H. Heinig, and W. Moller, Physical Review B **64** (2001).
19 M. Anderle and C. M. Loxton, Nuclear Instruments & Methods in Physics Research Section B-Beam Interactions with Materials and Atoms **15,** 186 (1986).
20 J. H. Son, H. B. Kim, C. N. Whang, and K. H. Chae, Applied Surface Science **233,** 288 (2004).
21 H. J. Fitting, L. F. Kourkoutis, B. Schmidt, B. Liedke, E. V. Ivanova, M. V. Zamoryanskaya, V. A. Pustovarov, and A. F. Zatsepin, Physica Status Solidi a-Applications and Materials Science **209,** 1101 (2012).
22 W. Moller and W. Eckstein, Nuclear Instruments & Methods in Physics Research Section B-Beam Interactions with Materials and Atoms **2,** 814 (1984).
23 W. D. Wilson, L. G. Haggmark, and J. P. Biersack, Physical Review B **15,** 2458 (1977).
24 O. S. Oen and M. T. Robinson, Nuclear Instruments & Methods **132,** 647 (1976).
25 J. Lindhard and M. Scharff, Physical Review **124,** 128 (1961).
26 P. Sigmund, Physical Review **184,** 383 (1969).
27 W. Möller and M. Posselt, Wissenschaftlich-Technische Berichte Forschungszentrum Rossendorf **FZR-317** (2001).
28 H. Hofsass, K. Zhang, and A. Mutzke, Applied Surface Science **310,** 134 (2014).
29 M. P. Seah and T. S. Nunney, Journal of Physics D-Applied Physics **43** (2010).
30 O. T. Mogi K., Suzuki M., J. Surf. Anal. **9,** 514 (2002).
31 H. H. Andersen, Applied Physics **18,** 131 (1979).
32 D. Marton, in *Wiley series in ion chemistry and physics* (Wiley, Chichester, 1994).
33 S. J. Zinkle and C. Kinoshita, Journal of Nuclear Materials **251,** 200 (1997).

34 P. Sigmund and A. Grasmarti, Nuclear Instruments & Methods **182,** 25 (1981).

35 B. Wang, Y. T. Yu, I. Pignatelli, G. Sant, and M. Bauchy, Journal of Chemical Physics **143** (2015).

36 J. S. Zhen, Q. Yang, Y. H. Yan, X. W. Jiang, S. A. Yan, W. Chen, and X. Q. Guo, Radiation Effects and Defects in Solids **171,** 340 (2016).

37 P. Sigmund, Applied Physics Letters **25,** 169 (1974).

38 D. Peak and R. S. Averback, Nuclear Instruments & Methods in Physics Research Section B-Beam Interactions with Materials and Atoms **7-8,** 561 (1985).

39 R. Collins, Radiation Effects and Defects in Solids **98,** 1 (1986).

40 W. Bolse, Materials Science and Engineering a-Structural Materials Properties Microstructure and Processing **253,** 194 (1998).

41 K. Nordlund, M. Ghaly, and R. S. Averback, Journal of Applied Physics **83,** 1238 (1998).

42 B. Park and H. Lee, Journal of Materials Research **14,** 281 (1999).

43 Y. T. Cheng, M. Vanrossum, M. A. Nicolet, and W. L. Johnson, Applied Physics Letters **45,** 185 (1984).

44 W. L. Johnson, Y. T. Cheng, M. Vanrossum, and M. A. Nicolet, Nuclear Instruments & Methods in Physics Research Section B-Beam Interactions with Materials and Atoms **7-8,** 657 (1985).

45 M. Vanrossum, Y. T. Cheng, M. A. Nicolet, and W. L. Johnson, Applied Physics Letters **46,** 610 (1985).

46 M. Strobel, K. H. Heinig, and T. Michely, Nuclear Instruments & Methods in Physics Research Section B-Beam Interactions with Materials and Atoms **178,** 105 (2001).

47 M. Strobel, K. H. Heinig, and T. Michely, Surface Science **486,** 136 (2001).

48 T. Muller, K. H. Heinig, and B. Schmidt, Nuclear Instruments & Methods in Physics Research Section B-Beam Interactions with Materials and Atoms **178,** 109 (2001).

49 T. Muller, K. H. Heinig, and B. Schmidt, Nuclear Instruments & Methods in Physics Research Section B-Beam Interactions with Materials and Atoms **175,** 468 (2001).

50 B. Liedke, K.-H. Heinig, and W. Moeller, Nuclear Instruments & Methods in Physics Research Section B-Beam Interactions with Materials and Atoms **316,** 56 (2013).

51 J. Kelling, G. Odor, M. F. Nagy, H. Schulz, and K. H. Heinig, European Physical Journal-Special Topics **210,** 175 (2012).

52 N. Metropolis, A. W. Rosenbluth, M. N. Rosenbluth, A. H. Teller, and E. Teller, Journal of Chemical Physics **21,** 1087 (1953).

53 W. Schweika, *Disordered Alloys – Diffuse Scattering and Monte Carlo Simulations* (Springer, Berlin, 1998).

54 M. Uematsu, H. Kageshima, Y. Takahashi, S. Fukatsu, K. M. Itoh, K. Shiraishi, and U. Gosele, Applied Physics Letters **84,** 876 (2004).

55 U. M. Gosele, Annual Review of Materials Science **18,** 257 (1988).

56 D. Mathiot, J. P. Schunck, M. Perego, M. Fanciulli, P. Normand, C. Tsamis, and D. Tsoukalas, Journal of Applied Physics **94,** 2136 (2003).

57 C. Haas, Journal of Physics and Chemistry of Solids **15,** 108 (1960).

58 B. Liedke, Thesis, Technische Universität Dresden, 2011.

59 G. Kissinger, M. A. Schubert, D. Kot, and T. Grabolla, Ecs Journal of Solid State Science and Technology **6,** N54 (2017).

60 W. Wijaranakula, Applied Physics Letters **59,** 1185 (1991).

61 H. Okamoto, Journal of Phase Equilibria and Diffusion **28,** 309 (2007).

62 A. Sarikov, in *Nanomaterials and Nanotechnology*, edited by W. Ahmed (One Central Press Ltd., 2016), p. 36.

63 A. M. Agarwal and S. T. Dunham, Journal of Applied Physics **78,** 5313 (1995).

64 M. Roussel, E. Talbot, R. P. Nalini, F. Gourbilleau, and P. Pareige, Ultramicroscopy **132,** 290 (2013).

65 S. M. Schnurre, J. Grobner, and R. Schmid-Fetzer, Journal of Non-Crystalline Solids **336,** 1 (2004).

66   S. Matteson, B. M. Paine, and M. A. Nicolet, Nuclear Instruments & Methods **182,** 53 (1981).
67   J. W. Cahn, Acta Metallurgica **9,** 795 (1961).
68   I. M. Lifshitz and V. V. Slyozov, Journal of Physics and Chemistry of Solids **19,** 35 (1961).
69   C. Wagner, Zeitschrift Fur Elektrochemie **65,** 581 (1961).
70   T. Mueller, Thesis, Technische Universität Dresden, 2005.